Optics & Laser Technology 143 (2021) 107241

Contents lists available at ScienceDirect

Optics and Laser Technology

journal homepage: www.elsevier.com/locate/optlastec

Full length article

Femtosecond and picosecond laser fabrication for long-term superhydrophilic metal surfaces

Rahul A. Rajan [a,b,d], Chi-Vinh Ngo [a,*], J. Yang [a], Yu Liu [a,b], K.S. Rao [a], Chunlei Guo [c]

[a] The GPL Photonics Laboratory, Changchun Institute of Optics, Fine Mechanics and Physics, Chinese Academy of Sciences, Changchun 130033, China
[b] University of Chinese Academy of Science, Beijing 100039, China
[c] The Institute of Optics, University of Rochester, Rochester, NY 14627, USA
[d] International School of Photonics, Cochin University of Science and Technology, Cochin 682022, India

ARTICLE INFO

Keywords:
Long-term superhydrophilic aluminum
Nano-microstructures formation
Femtosecond laser ablation
Picosecond laser ablation
Zeolite coating

ABSTRACT

This paper reports the femtosecond (fs) laser and picosecond (ps) laser fabrications to create superhydrophilic surfaces. Subsequently, investigations of the surface morphologies and the surface chemistry using EDS, XRD, and FTIR-spectroscopy are carried out. Due to significant variations in the formation of micro-nano structure and molecular compositions, fs laser and ps laser fabricated surfaces exhibited a noteworthy difference in surface wettability by controlling the laser parameters. It is evident from experimental results that ps laser structured surfaces show efficient superhydrophilic nature (0° contact angle with 300 ± 18 ms spreading time) than the fs laser (0° contact angle with 400 ± 18 ms spreading time) due to higher surface roughness factor and surface energy resulted from laser-induced thermalization. Nevertheless, all fabricated surfaces convert from superhydrophilic to superhydrophobic due to chemisorbed hydroxyl (–OH) and C–C(H) functional group contamination. An eco-friendly zeolite (Na-based ZSM-5) coating is used on such ultrafast laser fabricated surfaces to maintain the superhydrophilic property for more than 14 months. The proposed investigation provides an innovative approach for producing long-term stable superhydrophilic metal surfaces, which are useful for water treatment, microfluidics, and heat transfer applications.

1. Introduction

Superhydrophilic surface attracts researchers' attention for several years because of its engineering applications such as water treatment, water harvesting, water splitting nano/microfluidics, and self-cleaning [1–5]. The leaf structures of *Ruellia devosiana* [6], the wetting surface on carnivorous plants [7], spider webs, and water collecting body surface of desert beetles [8] are some naturally existing superhydrophilic surfaces. Many researchers fabricated the artificial nano/micro wetting surfaces using several conventional techniques such as thermal embossing, sol–gel, chemical etching, electrodeposition, and chemical vapour deposition [9–13]. However, poor mechanical properties of the surface structures, complicated procedures, and high fabrication costs make these conventional techniques less suitable for industrial applications [14]. In contrast, ultrafast laser fabrication of regular nano-microstructures under controlled experimental conditions (laser energy, laser scanning speed, laser pulse duration, and fabricated groove distance) has been employed as a more suitable industrial technique that allows precise tuning of surface wettability [15,16]. The better versatility of the laser fabrication technique permits it to use on almost all metals [17–27]. Earlier researchers fabricated a variety of micro-and nanostructures on various materials [28–32]. The fundamental principle is that material with rough micro-nano structured surfaces followed by high surface energy modification exhibits excellent superhydrophilicity.

However, these surfaces' superhydrophilic property is not stable in ambient environment conditions due to chemisorbed organic material contamination [33]. For example, it changes the surface from superhydrophilicity to superhydrophobicity within a short time, from a few weeks to a few months [30,34,35]. Yang et al. reported the wettability transition of nanosecond (ns) laser structured surface on Inconel alloy [15]. Additionally, Long et al. presented the ps laser structured surface on Cu due to the adsorption of atmospheric organic matters [36]. It indicates that the long-term stable superhydrophilicity of laser-ablated metal surfaces is still a challenging problem [37,38].

In this study, we compare the surface morphology and surface

* Corresponding author.
E-mail address: chivinh@ciomp.ac.cn (C.-V. Ngo).

https://doi.org/10.1016/j.optlastec.2021.107241
Received 11 February 2021; Received in revised form 15 April 2021; Accepted 11 May 2021
Available online 15 June 2021

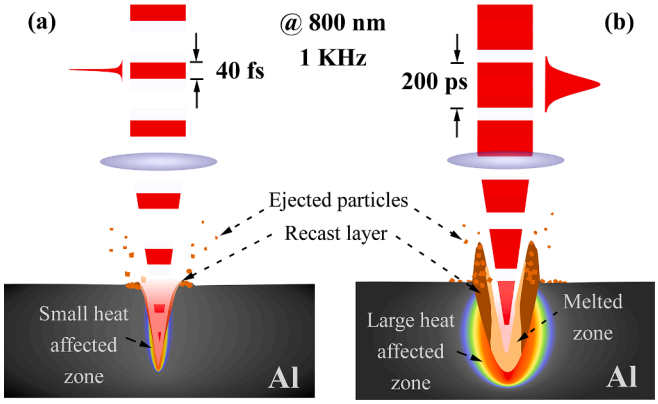

Fig.1. A schematic illustration of Al surface ablation using (a) fs and (b) ps laser pulses and formation of microgroove.

chemistry modification of structured superhydrophilic surfaces, which are fabricated independently by fs laser and ps laser. Herein, we used scanning electron microscopy (SEM), optical microscope analysis, energy-dispersive elemental spectroscopy (EDS), X-ray diffraction (XRD), infrared (IR) spectroscopy to study morphology and chemical composition of various laser fabricated surfaces. Studies confirmed that modulation of laser pulse width, power, scanning speed, and distance between two adjacent grooves (step sizes) precisely control the surface wettability. The effects of the formation of micro-nano structure and molecular compositions to achieve better superhydrophilic nature were also studied in detail. Finally, to maintain the superhydrophilic property for long-term usage, zeolite coating has been used. Interestingly, it keeps the superhydrophilic property for more than 14 months. It benefits several applications which solely depends on superhydrophilic property such as, filtering polluted solutions on sanitation system [1], increasing the solar/energy absorption [1], wicking liquids without the effect of gravity [39–42], and generating hydrogen energy [43]. As per the best of our knowledge, the proposed investigation is the first report comparing the fs laser and ps laser ablation for a long-term stable superhydrophilic surface with high performances.

2. Experimental materials and methods

2.1. Sample preparation

Aluminum (99.99% Al) sheets of 1.5 cm × 1.5 cm × 0.1 cm were used as fabrication samples. The samples were cut by high-speed metal cutting to avoid physical bending; subsequently, sandpaper (400 grifts) is used to polish the edges. Distilled (DI) water and ethanol were used to clean samples ultrasonically before and after the laser fabrication and dried with compressed air.

2.2. Femtosecond and picosecond laser texturing for superhydrophilic surfaces

In this research, two types of laser pulses (fs laser: 40 fs and ps laser: 200 ps) have a central wavelength of 800 nm and a repetition rate of 1 kHz employed to fabricate structures. Further, a comparison study has been made to find an effect of surface morphology and chemistry on surface wettability. The schematic layout of the Al surface ablation using fs and ps laser pulse train is illustrated in Fig. 1. The maximum fs laser power delivered is 6 W, which was attenuated using neutral density filters. Such appropriate laser power focussed on the sample with a spherical focal lens (f = 200 mm) along the z-axis. The ps laser pulse trained from the uncompressed radiation of Ti: Sapphire laser (Spitfire Ace, Spectra-Physics) is used to process the Al samples. The laser-fabricated area on the sample surface was controlled into 3 mm × 3 mm with a programmed 3-D translational stage. The employed laser parameters (power, pulse duration, scanning speed) and groove spacing for this research are shown in Table 1. After laser processing, all the fabricated samples were kept in an ambient atmosphere to check their reaction with the actual atmospheric condition.

Table 1
The experimental conditions used in this study.

	fs laser	ps laser
Pulse width	40 fs	200 ps
Laser power (mW)	40, 80, 120	
Laser scanning speed (mm/s)	0.1, 0.25, 0.5, 0.75, 1.0, 1.25, 1.5, 1.75, 2.0, 2.5, 3.0, 4.0, 5.0	
Groove spacing (μm)	20, 60, 110, 160	

2.3. Hydrothermal In-situ crystallization of zeolite for stable superhydrophilicity

The uniform zeolite coating on intricate laser fabricated Al structures achieved by in-situ crystallization technique. A hydrothermal Teflon-lined autoclave reactor is used as a container for in-situ crystallization. The synthesis solution for Zeolite Socony Mobil–5 (ZSM-5) was prepared by a method introduced by Cheng et al. [44]. Its molar composition is 16TPAOH:0.64NaOH:1TEOS:92H_2O:0.0018Al, where TPAOH and TEOS stand for tetrapropylammonium hydroxide and tetraethylorthosilicate, respectively. Al foil (0.0105 g) was added to the NaOH solution (5.36 g of NaOH and 336 mL DI water) and stirred for 10 h for the complete dissolving. Further, 30 mL of TPAOH and 45 mL of TEOS were added dropwise to the prepared solution. Again, the clear solution was stirred overnight at room temperature [45].

2.4. Measurement and surface characterization

A contact angle meter (JC2000D3, POWEREACH, China) was used to measure the surface wettability. The static contact angles of the DI water droplet on sample surfaces were measured by placing the samples on a flat, smooth, and clean surface in line with a camera. The camera is placed parallel to the grooves for each measurement. Each water droplet of 1 μL volume was carefully placed on the sample surface using the dispense function in the software. Images were taken after water droplets left on the sample surfaces for a few seconds. Then droplets were blown away using a compressed air blower, and the surfaces were dried thoroughly for conducting the next test. All these measurements were performed at room temperature. The surface morphology and surface chemistry of fabricated samples are analyzed by a 3D Laser Scanning Microscope (VX-series, Keyence, Japan), an X-ray diffraction measurement (D8, Bruker, Germany), a Scanning electron microscope (S-4800, Hitachi, Japan), a Fourier-transform Infrared (Cary 630, Agilent, United States) spectroscopy, and an energy-dispersive x-ray spectroscopy (ProX-5, Phenom, Netherlands).

3. Results and discussion

3.1. Effect of surface roughness factor on wettability

According to the Wenzel model, the apparent contact angle of a water droplet on a rough surface as:

$$\cos\theta_r = r\ \cos\theta_f \quad (1)$$

Where, θ_r is the apparent contact angle, θ_f is the contact angle on the flat surfaces, r is the surface roughness factor, which is the ratio of actual surface area (A_{actual}) to the geometrical surface area ($A_{geometric}$), $r = A_{actual} / A_{geometric}$ [46]. As the roughness factor increases, wettability changes from hydrophobic to more hydrophobic or from hydrophilic to more hydrophilic. Hence, to achieve complete wetting property or

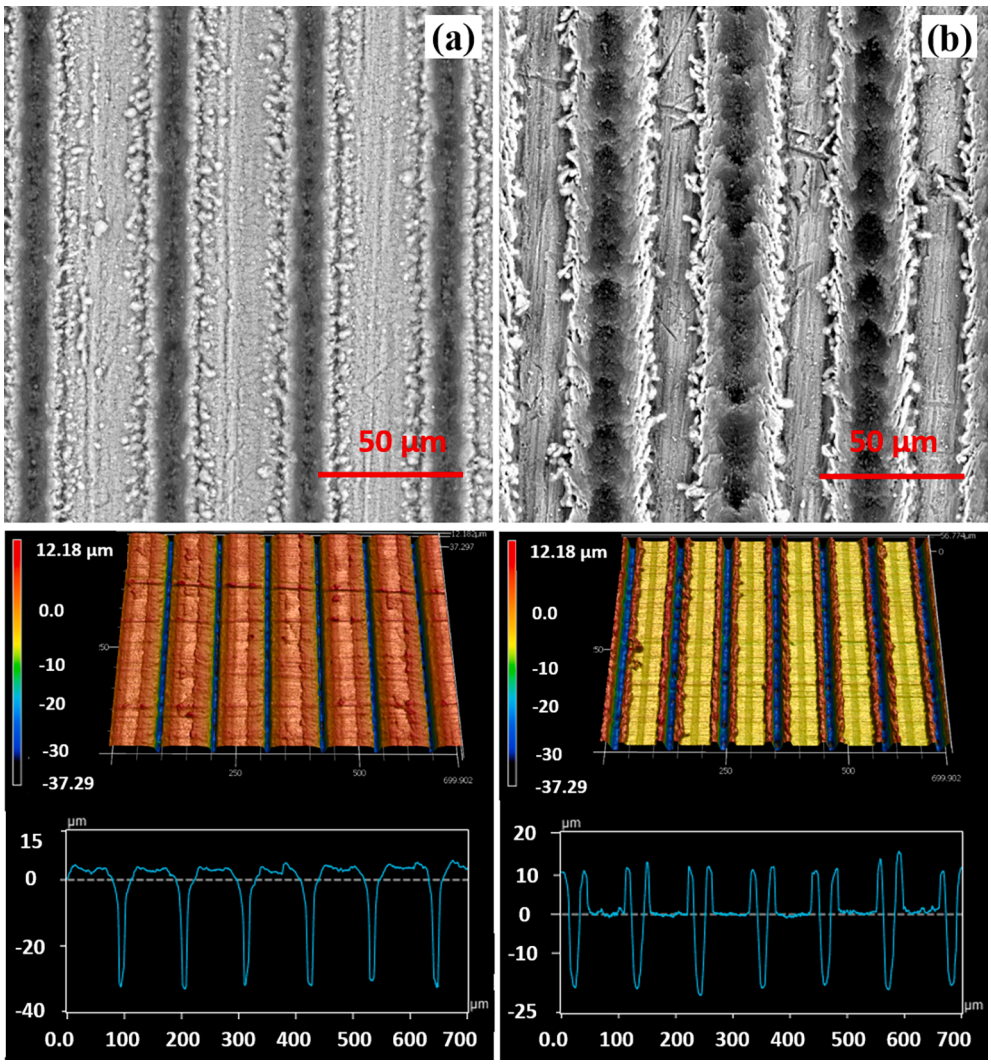

Fig. 2. The pulse width effect of fabricated structure's SEM image (top row), optical microscopic image (middle row) and its line profile (bottom row) (a) femtosecond laser and (b) picosecond laser.

superhyrophilic property, the surface roughness factor of the Al sample is increased by pulsed laser microgroove structuring. Here, the pulse duration, laser power, scanning speeds, and step sizes are vital factors to control the roughness factor. The contact angle of flat and laser-ablated Al surfaces is shown in Fig. S1.

3.1.1. *Effect of laser pulse duration*

In pulsed laser-matter interaction, the pulse duration is one of the prime laser parameters that determine the energy transfer from a photon to the interacting material. In the case of metal, a large number of free electrons will absorb a part of the interacting energy of the laser pulses during its interaction time. Hence, by changing the pulse duration, laser ablation can be controlled, thus inducing microstructure morphology. In this study, we used two lasers of 200 ps and 40 fs for creating microgroove capillary channels and compared its surface morphology and surface chemistry dependence on wettability.

Due to longer pulse duration, ps laser fabrication is associated with a significant thermalization process, with surface melting, evaporation, and melt expulsion at adequate laser fluences, depending on the material properties such as absorption coefficient, thermal conductivity, and thermal diffusivity. In this scenario, the thermal diffusion effect demands significant importance for comparing the thermal effect induced by fs laser and ps laser. The thermal penetration depth (d) due to different laser pulse width can be calculated by $d=\sqrt{D \times \tau}$ (where D is the thermal diffusivity $= K/\rho C_p$ and τ is the pulse width of the laser used for fabrication). The calculated thermal penetration depth of the ps laser (200 ps) was 13.92 µm. The optical penetration depth (1/absorption coefficient or $\lambda_0/ 4\pi \times k$; where λ_0 is the central wavelength of the laser used for fabrication and k is the extinction coefficient) of 800 nm on an aluminum substrate is around 7.58 nm. As the thermal penetration is much greater than the optical penetration length, ps laser fabrication is dominated by the thermalization process. It led to thermal ablation with a large heat-affected zone (HAZ) and resulted in melted microgrooves with a large amount of ablation debris and surface protrude recast layer (shown in Fig. 2b).

Nevertheless, this classical explanation of laser-matter interaction failed their validity for explaining fs laser ablation. Upon fs laser irradiation on a metal surface, part of the laser energy is absorbed by free electrons through the inverse Bremsstrahlung [47]. The ultrashort pulse width of the fs laser, which is shorter than the electron–phonon/ion relaxation time (~1 – 10 ps), causes thermal nonequilibrium between the electron and lattice subsystems. Therefore, the energy evolution in the metal is explained by the two-temperature model [48]. When the energy of the electron subsystem is large enough, a direct solid to vapour transition takes place. These mechanisms associated with fs laser ablation led to non-thermal ablation, reducing the HAZ in the ablated material [30,47,49]. It resulted in fs laser fabricated microgrooves with clean edges and less recast formation (shown in Fig. 2a) compared to ps

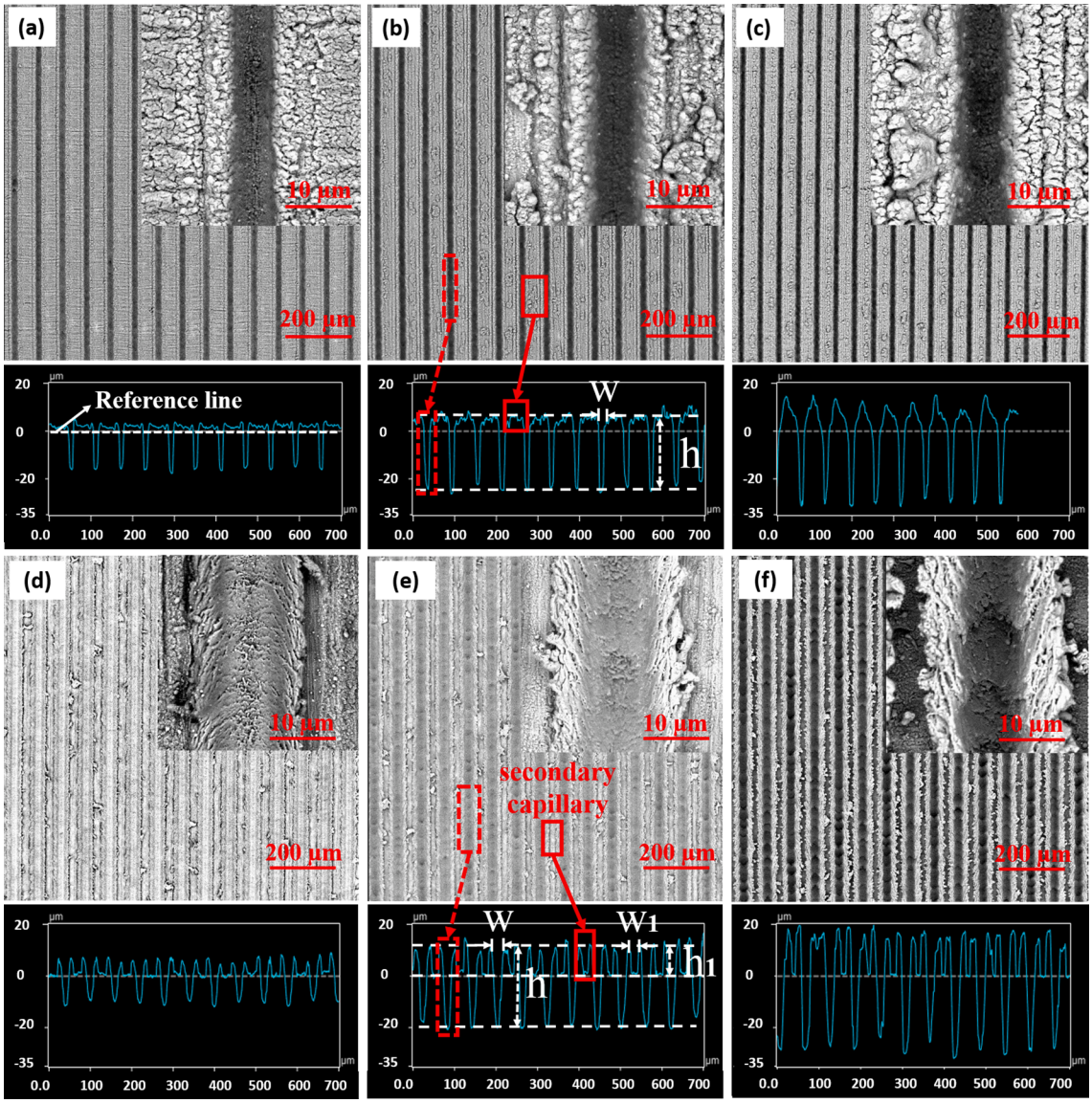

Fig. 3. SEM images (top) and its surface line profile (bottom) for ablated grooves at different laser powers. For fs laser ((a) 40 mW (b) 80 mW and (c) 120 mW) and ps laser ((d) 40 mW (e) 80 mW and (f) 120 mW), respectively.

laser fabricated microgrooves. Therefore, according to Eq. (1), the water droplet placed on the ps laser fabricated sample experienced more contact surface area, leading to better superhydrophilicity than the fs laser fabricated sample. The contact surface area (or actual surface area) and surface roughness factor calculation of fabricated surfaces were performed using two simplified 3D models as shown in supporting information (Fig. S2).

3.1.2. *Effect of laser power*

The laser power determines the aspect ratio (the depth (h) to opening width (w) ratio) of fabricated microgrooves. Fig. 3(a, b, c) and Fig. 3(d, e, f) show the microgrooves fabricated by different fs laser and ps laser powers, respectively. Scanning-speed and step size kept constant at 1.0 mm/s and 60 µm respectively throughout the experiment. To calculate the aspect ratio, h and w of fs and ps laser fabricated microgrooves are measured directly from the 2-D surface profile as shown in Fig. 3. Aspect ratio of samples are measured by taking the average peak depths and widths of around ten different microgrooves. As shown in SEM images, fs laser fabricated capillary grooves (marked by dashed rectangular boxes in Fig. 3 (b)) are smooth and regular compared to the grooves created using ps laser (marked by dashed rectangular boxes in Fig. 3 (e)). It resulted in deep capillary channels with less ablated recast deposition (above the reference line; marked by solid rectangular boxes in Fig. 3 (b)). At 40 mW and 80 mW fs laser power, the thickness of such recast deposition is measured less than 5 µm, whereas it is around 15 µm at 120 mW. Besides, when the laser power increase, the ablated groove depth (h) also gradually increase, where the microgroove width (w) is almost consistent. Consequently, it helps to improve the aspect ratios of fs laser fabricated surfaces by increasing h. In the case of ps laser fabricated surfaces, due to the pulse width effect, fabricated surfaces were formed with more debris and recast deposition on the surface. It creates an additional microgroove capillary (with depth, h1, and opening width, w1), which can be called secondary capillary made of recast deposition from the adjacent microgrooves as the side walls (marked by solid rectangular boxes in Fig. 3 (e)). It is evident from ps laser fabricated surface's 2-D surface profile and SEM images, as increase the laser power, ablation recast deposition is more, thus h1 increase gradually, whereas, due to a large amount of ablation recast deposition, the opening width (w1) of secondary microgroove channel reduce.

Hence, the aspect ratio of secondary microgrooves also increases gradually with respect to different laser powers. It increases the total aspect ratio of ps laser fabricated microgrooves, which is calculated by

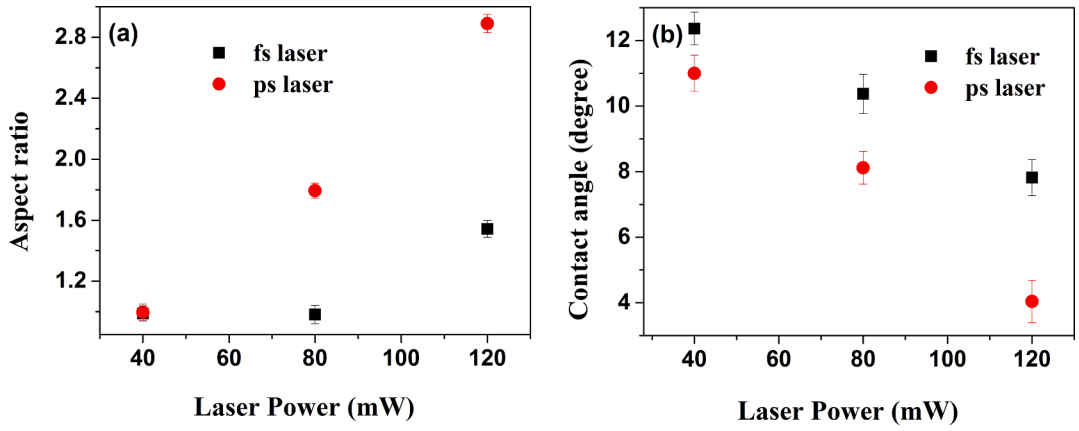

Fig. 4. The relation between laser power and: (a) aspect ratio and (b) contact angle.

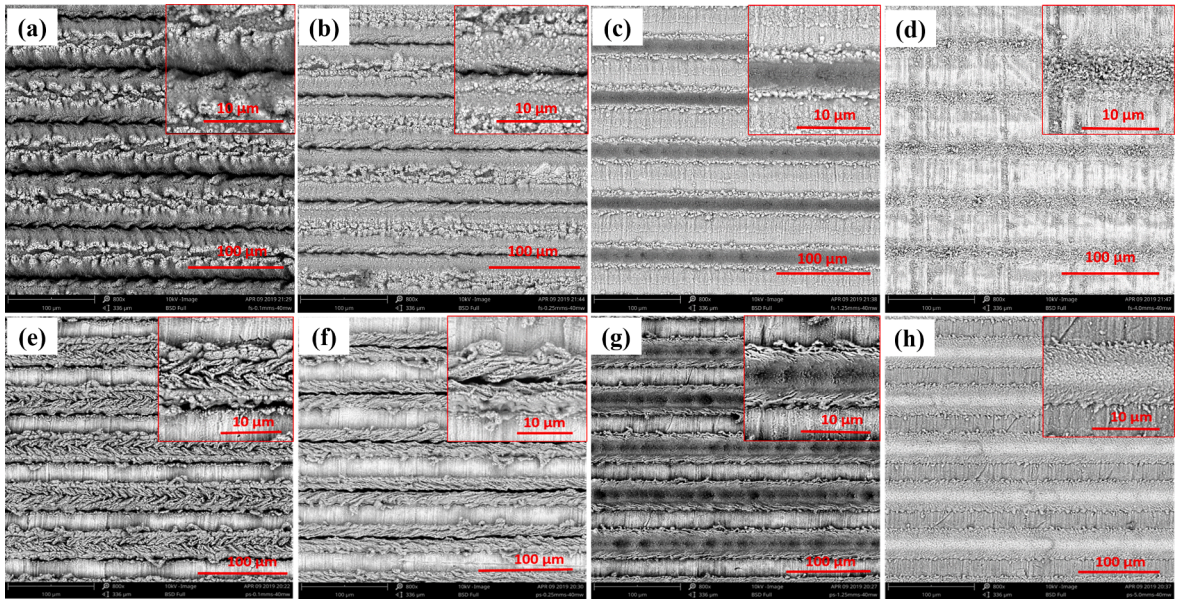

Fig. 5. fs laser (a-d)and ps laser (e-h) ablated microgrooves with different scanning speed: (a,e) 0.1 mm/s (b,f) 0.25 mm/s (c,g) 1.0 mm/s (d,h) 5.0 mm/s.

summing up the individual aspect ratios of the directly fabricated microgrooves and secondary microgrooves. Hence, according to the Wenzel model, actual surface area as well as overall surface roughness increased. In the case of fs laser fabrication, secondary microgrooves are absent due to smaller surface protrude recast deposition at considered laser powers. Therefore, as shown in Fig. 4 (a), the overall aspect ratio of ps laser fabricated surface is higher than that of the fs laser fabricated surfaces.

The water wicking effect of the secondary microcapillaries plays an essential role in determining the overall superhydrophilicity of fabricated surfaces, and a similar observation is made by *Chengyun Zhang et. al.* with high energy fs laser processing [50]. Fig. 4(b) shows the contact angle variation of fabricated surfaces measured at different fs and ps laser powers. Due to the combined effect of higher surface roughness factor and the wicking action of both secondary capillaries (formed through recast deposition) as well as the directly fabricated capillaries, water droplets on ps laser fabricated surfaces exhibit lower contact angles than those on fs laser fabricated surfaces.

3.1.3. *Effect of scanning speed*

In this section, we analyze the morphology and wettability of samples with respect to different scanning speeds (0.1, 0.25, 0.5, 0.75,1.0, 1.25,1.5,1.75, 2.0, 2.5, 3.0, 4.0, and 5.0 mm/s) at fixed laser power (120 mW) and stepsize (60 µm). Scanning speed determines the number of pulse accumulation or the pulse overlapping on the sample. The percentage of pulse overlapping in the direction of scanning is estimated by (1-*S*/spot size) × 100, where *S* is the spacing between two adjacent laser spots equals the ratio of scanning speed to the laser frequency. The laser spot size was calculated as 51 µm for both fs laser and ps laser beams at the focal spot. The percentage of pulse overlapping for various scanning speed used in this study (for 1 kHz laser repetition rate) are as follows: 0.1 (99.8%), 0.25 (99.5%), 0.5 (99.01%), 0.75 (98.5%), 1.0 (98.03%), 1.25 (97.54%), 1.5 (97.05%), 1.75 (96.56%), 2.0 (96.07%), 2.5 (95.09%), 3.0 (94.11%), 4.0 (92.15%) and 5.0 mm/s (90.19%).

Fig. 5 shows fs laser and ps laser ablated Al surfaces with different scanning speeds 0.1, 0.25, 1.0, and 5.0 mm/s. The lower scanning speed (0.1 to 0.5 mm/s) results in excessive laser exposure at one particular point on the surface, resulting in an increased thermal effect because of its large initial incident fluence. Such large fluence leads to improved material ablation process and consequently paybacks deeper but narrowed micro-groove capillary channel. However, the sub-micron structure formation due to the material re-condensation [51] makes the capillary channels in non-uniform shape (showed in Fig. 5 (a, b, e, and f). At lower scanning speeds with a high repetition rate, the incubation effect also plays an essential role in forming many sub-micron ripple structures and nano-capillary channels throughout the microgrooves

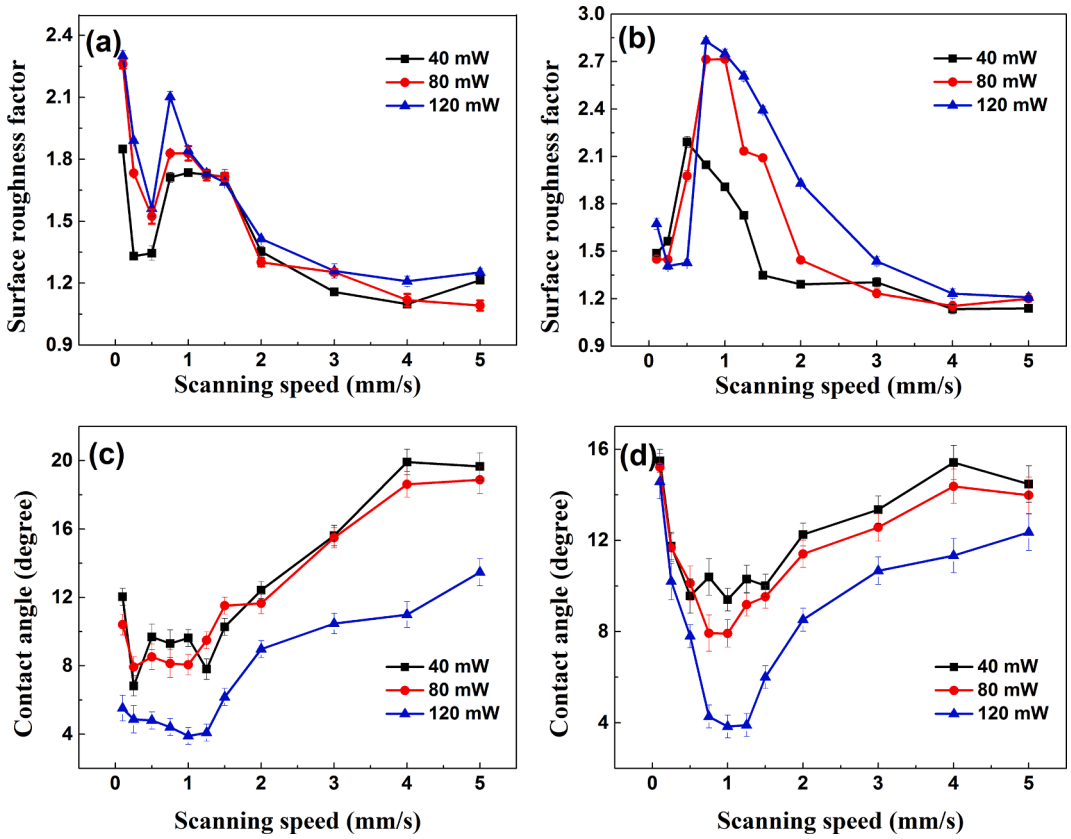

Fig.6. Effect of laser scanning speed on the surface roughness factor and contact angle for different laser power; (a and c) fs laser fabrication results (b and d) ps laser fabrication results.

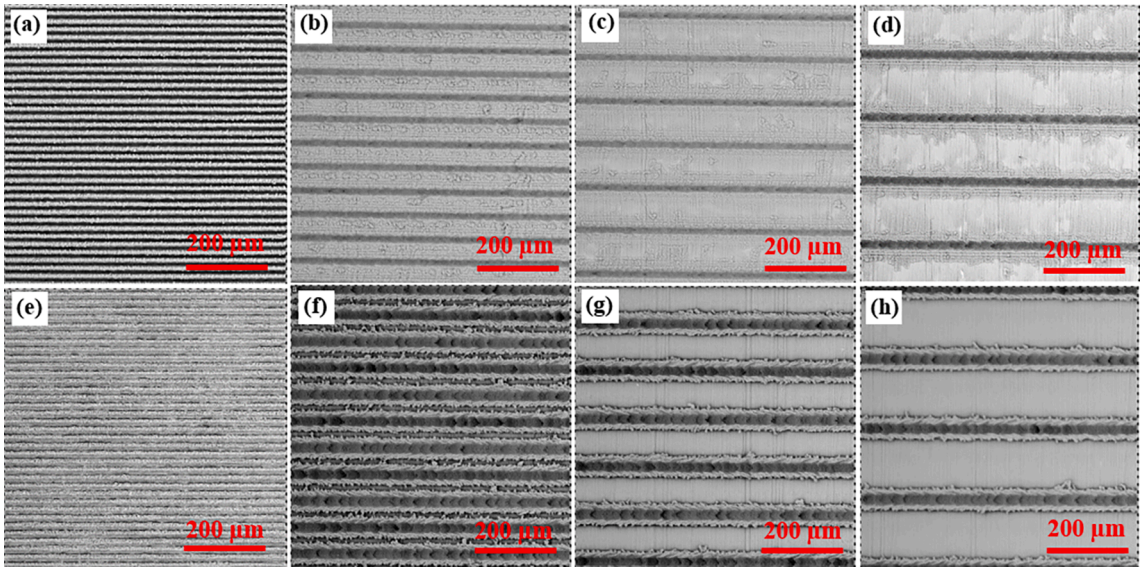

Fig. 7. Surface morphology of fs (a- d) and ps (e- h) laser fabricated surfaces with different step sizes (a, e: 20 µm, b, f: 60 µm, c, g: 110 µm and d, h:160 µm).

[52]. Such complex structures reduced the overall aspect ratio and surface roughness factor of those fabricated grooves (Fig. 6 (a,b)). According to previous studies, it significantly limits the capillary flow rate and the spreading factor across the surface than the uniform channels, similar results were reported as the slowing down spreading and liquid drop progression in non-uniform capillary channels [53–55].

The wetting nature of the fabricated surfaces at various scanning speeds (0.1 mm/s, 1.0 mm/s, and 5.0 mm/s) is evaluated by measuring water droplet contact angles. The contact angle information (Fig. 6(c,d)) on the surfaces shows that irregularly microstructured surfaces fabricated with 0.1 mm/s to 0.5 mm/s laser scanning speed results in a comparatively higher contact angle than the regular counterparts. Furthermore, at the higher laser scanning speed (i.e., 1.5 to 5.0 mm/s), the amount of laser exposure at a particular point is reduced, thus reducing the material ablation, resulting in a considerably reduced micro groove depth. As a result, the roughness factor of the whole

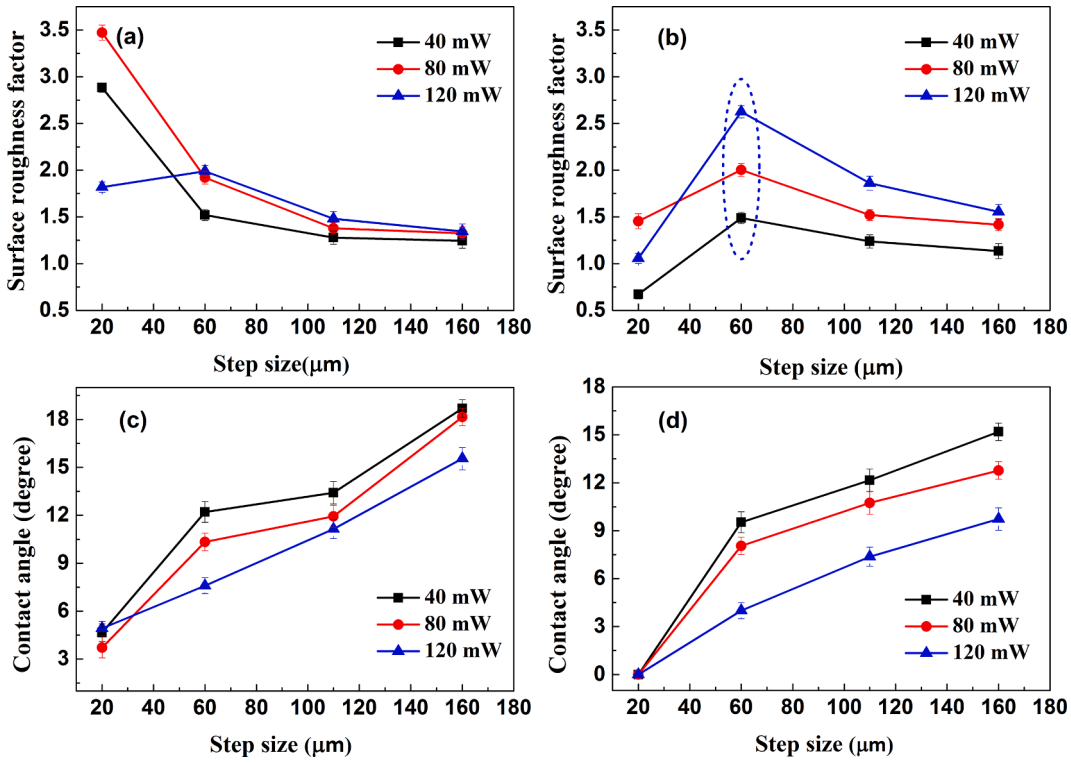

Fig. 8. Effect of different step size on the fabricated surface roughness factor and contact angle for different laser power for (a,c) fs laser fabrication and (b,d) ps laser fabrication.

fabricated area and overall surface wettability was reduced. However, the moderate laser scanning speeds (0.75, 1.0, and 1.25 mm/s) showed less formation of sub-micron structures across the fabricated grooves and formed smooth and uniform capillary channels with a higher aspect ratio (shown in Fig. S3) and increase the surface roughness factor. Thus, these scanning speed ranges confirm that regular, uniform, and high-aspect-ratio microgroove capillaries show better superhydrophilicity than the irregular and non-uniform capillary channels fabricated with fs laser and ps laser ablation techniques.

3.1.4. *Effect of step size*

This section has chosen the optimum laser scanning speed of 1 mm/s and studied three different laser powers (40 mW, 80 mW, and 120 mW) by varying the groove spacing (step size) to study its effect on the surface roughness and wettability. Fig. 7 shows the fs and ps laser fabricated surface morphology at 40 mW, with different step sizes.

The roughness factor of the laser fabricated surfaces is measured using the Wenzel model mentioned before. Fig. 8 shows the surface roughness factor and surface wettability (contact angle) of laser fabricated samples at a fixed scanning speed of 1 mm/s with laser powers of 40, 80, and 120 mW concerning different step sizes. Typically, the surface roughness factor increased with smaller grove spacing for both fs laser and ps laser fabricated surfaces. Nevertheless, the large thermalization associated with the ps laser fabrication (results in large HAZ) cause overlapping of adjacent grooves with the laser ablated recast debris and leads to a decrease in the aspect ratio (shown in Fig. S4 (a)) as well as surface roughness factor at 20 μm step size (shown in Fig. 8 (b)). It was similar in the case of high power fs laser (120 mW) fabricated surfaces at smaller step sizes (shown in Fig. S5 (b)). However, smaller thermalization and more minor ablated debris associated with low power fs (40 mW and 80 mW) laser fabrication (results in smaller HAZ) give distinct and overlap-free microgrooves, as shown in Fig. S5 (a). Therefore, 40 mW and 80 mW fs laser fabricated surfaces show a higher roughness factor than the 120 mW. As shown in Fig. 7 (b-d and f-h), when step sizes are at 60 μm or more, adjacent microgrooves are not

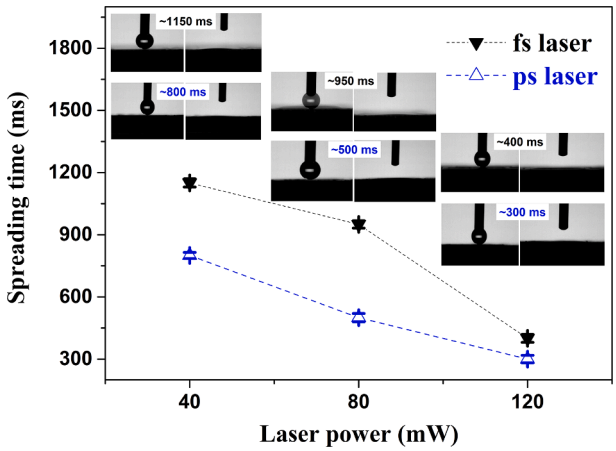

Fig. 9. Spreading time of water droplet on fs and ps laser fabricated surfaces with 20 μm step size (captured with high frame rate camera). Inset shows the droplet just before touching the surface and after forming thin film with their respective spreading time (top: on fs laser fabricated surfaces, bottom: on ps laser fabricated surfaces).

overlapping each other due to less recasting debris, notably in the case of ps laser fabricated surfaces recast debris deposit sideways of microgrooves and form a secondary microgroove capillary as discussed in Section 3.1.2. It increased the surface roughness factor of ps laser fabricated surfaces dramatically (marked with a dotted line in Fig. 8 (b)). After that, as we increased the step size, the secondary microgroove aspect ratio and the actual surface area or surface roughness factor decreases gradually.

Even though the roughness factor is a little lower at 20 μm step size, ps laser fabrication samples possess better superhydrophilicity due to increased amount of uneven nano-particles and micro-cracks (see, Fig. S4) with strong micro-capillary force, which is sufficient enough to

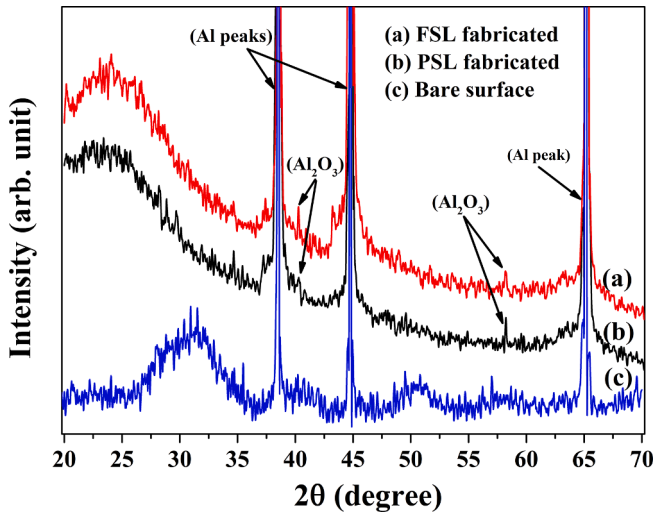

Fig. 10. XRD peak analysis; (a) fs laser fabricated surface and (b) ps laser fabricated surface with 120 mW laser power and 60 μm step size.

spread a water droplet all over the surface quicker [56]. The wetting differences in terms of spreading time of these nano-particles and micro-crack rich surfaces and others are calculated using a droplet size of 1 μL water (shown in Fig. 9). The result shows that ps laser-ablated Al surface with 120 mW and 20 μm step size spread the water droplet to achieve 0° contact angle and formed a thin layer in around 300 ms with ± 18 ms error bar, it confirmed by repeating the measurement at five different positions on the sample. The result is 1.66 times and 2.66 times faster than the surfaces fabricated with 80 mW and 40 mW laser power, respectively, and 1.33 times faster than the fs laser fabricated surfaces at 120 mW laser power and at 20 μm step size. It confirms that laser structured surfaces containing nano-particles and micro-cracks increase the fast-spreading, implying efficient superhydrophilic surfaces.

Overall, the studies for different laser powers, scanning speeds, and groove spacing provide the optimum parameters to fabricate the efficient superhydrophilic surfaces: 120 mW laser power, 0.75 to 1.25 mm/s scanning speed 20 μm- 60 μm groove spacing.

3.2. *Effect of surface chemistry on wettability*

In addition to micro-nano surface structures and surface roughness factors, a local change in surface chemistry is also an essential factor determining the superhydrophilicity of the surface. In this section, the difference in surface chemistry of fabricated samples with various laser parameters and its effect on superhydrophilicity was analyzed. The water drop will preferably spread on the high surface energy areas. Hence, highly oxidized laser fabricated surfaces with high surface energy could probably be complete wetting surfaces [33,57].

A detailed comparison of surfaces fabricated with different laser power, step size, and scanning speed has been made with the EDS analysis. The ratio of Al to O (Al/O) content measured on the laser fabricated surface was considered as the prime factor to determine the amount of oxidation. For instance, the lower the Al/O ratio, the higher the amount of oxidation leads to more elevated surface free energy, which results in better superhydrophilic behavior [33,57]. The Al/O ratio on the bare surface was measured as 10.68. For both fs laser and ps laser fabrication, the oxidation percentage was gradually increasing with an increase in laser power, smaller step sizes, and low scanning speeds (the corresponding weight percentage of Al, O, and Al/O ratio of fabricated surfaces are provided in table S1, S2, and S3 of supplementary file). The high oxygen content leads to an excellent polar aluminum oxide layer on fabricated surfaces, predominant in ps laser than fs laser.

Also, the formation of the Al_2O_3 layer is confirmed by XRD measurements. Fig. 10 (a), (b), and (c) shows the XRD data for fabricated samples at 120 mW, 1.0 mm/s, and 60 μm for fs laser, ps laser as well as bare Al surface, respectively. The diffraction peaks corresponding to Al_2O_3 at (40.99° and 58.35°) on laser fabricated surfaces were marked [58]. However, not much difference was observed from XRD analysis on the surface chemical composition between the two laser fabricated surfaces.

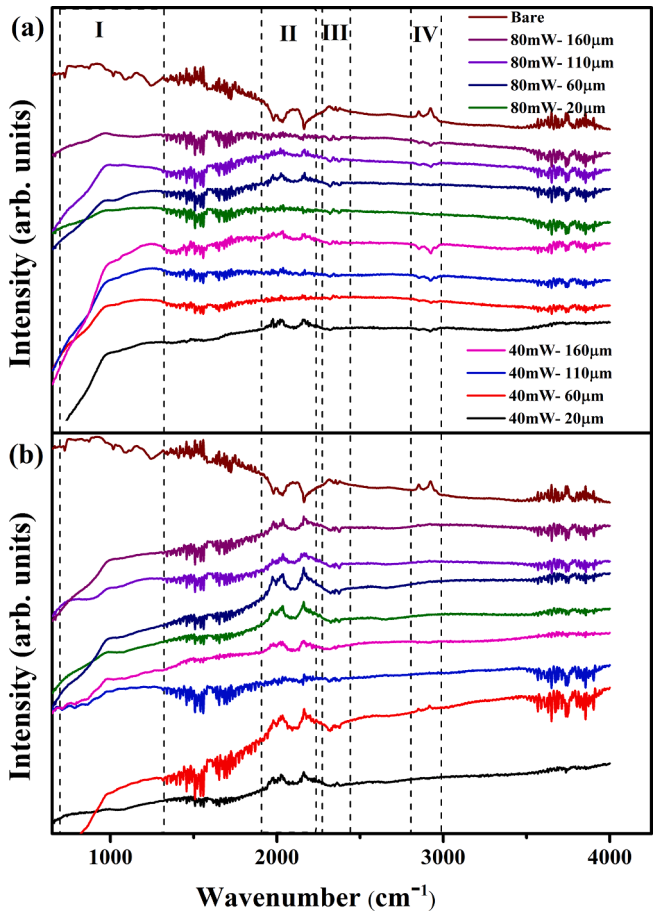

Fig. 11. FTIR spectrum of laser fabricated surfaces with different laser power and step sizes; (a) FS LASER fabricated surfaces, (b) PS LASER fabricated surfaces.

The fabricated surfaces could easily change their surface chemistry due to the airborne hydrocarbon depositions. The absorption capability of organic matters from the ambient air to the Al_2O_3 surface was enhanced due to abundant hydroxyl (–OH) functional groups [28,35]. It is observed that fabricated surface consists abundant of hydrocarbon molecular bonds. IR response of various molecular bonding in each fs laser fabricated surfaces (shown in Fig. 11 (a)) and ps laser fabricated surfaces (shown in Fig. 11 (b)) with laser power of 40 and 80 mW, and the step sizes of 20, 60, 110 and 160 μm were measured. In the case of bare Al, various strong C-H bending bonds (755 cm^{-1}) and weak $–CH_3$ groups (1355 cm^{-1}) are present [59]. However, after laser fabrication, these lines are absent (region (I)). It might be due to the decomposition of various organic elements due to high intense laser fabrication. Moreover, the medium C-H stretching of alkane group between 2840 cm^{-1}-3000 cm^{-1} range (region (IV)) [60] was observed on bare Al surface. In contrast, the high intense fs laser fabrication dissipates it and leads to the formation of stretching bonds of $–CH_2$- (2928 cm^{-1}), $–CH_3$ (2961 cm^{-1}), and C-H (2856 cm^{-1}) [58]. In contrast, instead of new bond formation, ps laser fabricated surfaces detected with the less intense peak of medium C-H stretching alkane functional groups centered around 2880 cm^{-1}. This difference due to the longer pulse

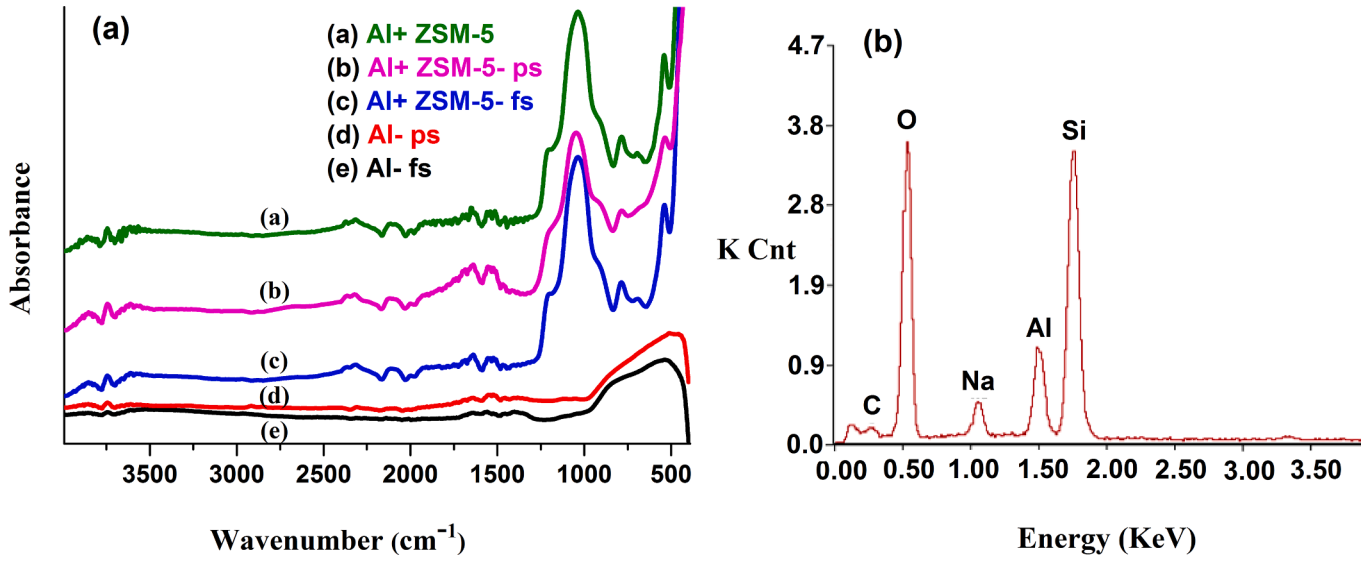

Fig. 12. (a) IR spectra and (b) EDS spectra of ZSM-5 (on bare sample).

duration of the ps laser, as discussed in Section 3.1. Also, in the case of laser fabricated surfaces, additional weak C-H bending (1985 cm^{-1}) [61] and weak C≡C stretching of alkyne functional groups (2093 cm^{-1}) [62] are observed (region (II) in Fig. 11). These functional groups are more intense for fs laser fabricated surfaces at 40 mW, 20 μm and 80 mW, 60 μm. However, in ps laser fabricated surfaces, the same functional groups are high intensity at step size 60 μm (at 40 and 80 W). As we discussed in Section 3.1.3 and 3.1.4, these laser parameter combinations had a larger laser exposed area and higher surface roughness factor. Hence, it is clear that the fabricated surfaces with more elevated roughness factors contain a significant amount of hydrocarbon chains (C-C(H)). Such C-C(H) functional groups exhibit excellent non-polar bonds, consequently reducing the surface free energy and increasing superhydrophobicity. Besides, region (III) in Fig. 11 shows that fabricated samples have a strong O = C = O stretching bond (2349 cm^{-1}), which is evidence of the trapping of CO_2 inside the microgrooves [63]. This bond's stretching was higher for 80 mW surfaces than the 40 mW surfaces in both fs laser and ps laser fabrication. Due to the higher aspect ratio of microgrooves at high laser power (as discussed with Fig. 5 (a) in Section 3.1.2.). As time progresses, such higher aspect ratio grooves will be modified as air pockets. As a result, the fabricated surface's wettability transforms from superhydrophilic to superhydrophobic. It shows the inevitability of maintaining clean and higher surface energy laser fabricated surfaces to obtain better superhydrophilicity. Nevertheless, the contamination of laser fabricated surfaces employed in the open-air application is unavoidable. The following section shows the wettability transition of such contaminated laser fabricated surfaces in a few weeks and the necessity of an efficient chemical coating to keep its super wetting nature for a long time.

3.3. Zeolite coating for stable superhydrophilicity

The surface transition of laser fabricated surfaces from superhydrophilic to superhydrophobic in a short period (5 weeks) has been considered an unavoidable phenomenon. Fig. S6 (b, d) shows the fabricated samples' non-wetting properties after five weeks. This state is widely known as Cassie state [64]. The chemisorbed organic molecules and decomposition of CO_2 into carbon and its components on the surface could be the critical factor for this wettability transition [25,65,66]. As shown in Fig. S6, the significant amount of carbon detected on the fabricated surface, which gives the primary evidence of surface contamination. Both fs laser and ps laser fabricated surfaces show the contact angle transition from 7.5° to 140.63° and from 4.5° to 150°,

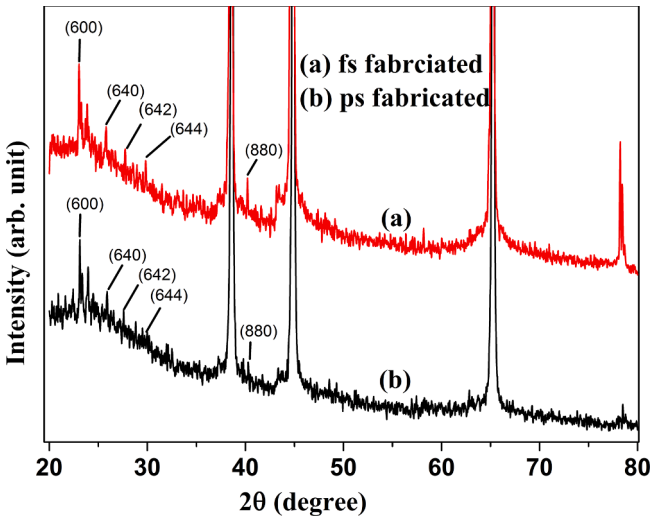

Fig. 13. XRD characteristic peaks of Na based ZSM-5 coating; (a) on fs laser fabricated surface and (b) on ps laser fabricated surface.

respectively, with a 2° error bar.

Such wettability transition was solved by coating Na-based ZSM-5 on the fabricated surfaces. It is an aluminosilicate of crystalline structure with uniformly distributed molecular-sized pores based on a 3-D network of O ions responsible for its water imbibition [67,68]. The molecular formula of the zeolite compound is $Na_2O{\cdot}Al_2O{\cdot}xSiO_2{\cdot}yH_2O$. The constituent particle NaOH was responsible for the presence of Na. Similarly, to achieve strong adhesion on substrates and reduce the intercrystal porosity structural direct agent TPAOH (tetrapropylammonium hydroxide) was used [45].

The structural properties of zeolite coating have been characterized using infrared spectroscopy and XRD analysis. IR spectra of bare and laser fabricated surfaces with and without zeolite coatings plotted in Fig. 12(a). The IR spectra of bare, fs laser and ps laser fabricated surface coated with zeolite (denoted as; Al + ZSM-5, Al + ZSM-5-fs, and Al + ZSM-5-ps, respectively) shows almost the same absorption peaks centered at 1100 cm^{-1}, 760 cm^{-1}, and 500 cm^{-1}. They are similar to the skeletal vibrations of MFI zeolite structures (of ZSM-5) due to the addition of TPAOH [69]. Due to the highly porous structure of ZSM-5, a weak broad IR band was observed at 960 cm^{-1}, which confirms the ZSM-

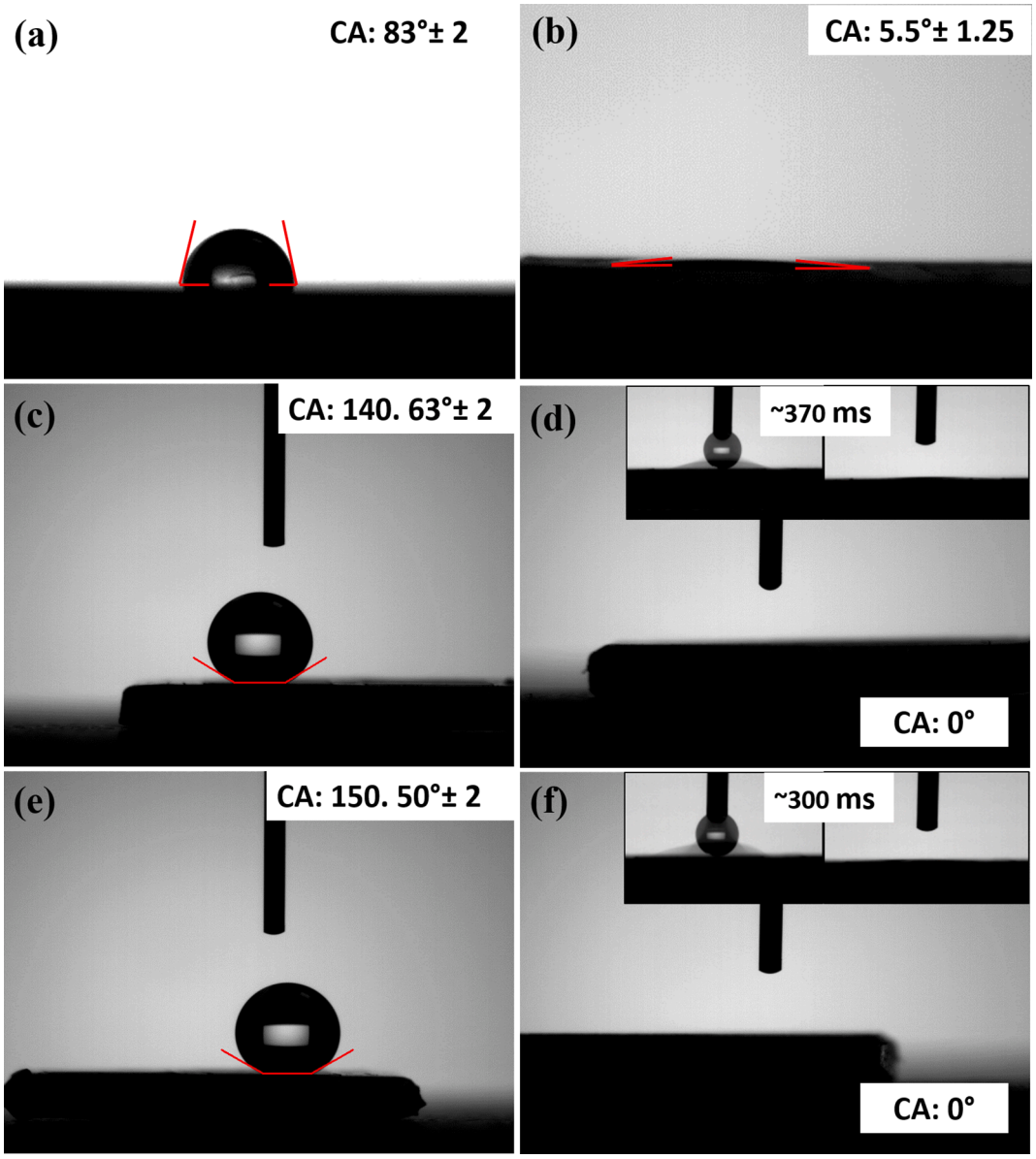

Fig. 14. Surface wettability transformation happened to the bare and laser fabricated surface after ZSM-5 coating: (a, b) Bare sample before after coating (c, d) fs laser fabricated surface before and after coating, and (e, f) ps laser fabricated surface before and after coating. (Inset figure shows the spreading time on the surfaces).

5 is highly hydroxylated. This absorption indicates the localized Si-OH stretching mode in SiO_3 –OH group [70]. The presence of asymmetric stretching bands at 950 cm^{-1} to 1250 cm^{-1}, stretching bands at 700 cm^{-1} to 1100 cm^{-1}, and the medium narrow peaks at 500 to 650 cm^{-1} correspond to the double ring pentasyl framework composed with the MFI type zeolite [71]. The EDS data presented in Fig. 12 (b) confirmed the formation of zeolite compound ZSM-5 on bare Al sample with higher silicon to an Al ratio (Si/Al) of 4.24, a fundamental property to these compounds.

Fig. 13 shows the characteristic XRD peaks and diffraction planes of Na-ZSM-5 on laser fabricated surfaces in the 2θ range of 20°- 80°. Some strong peaks from the Al substrate were also present due to the high penetration of X-rays. However, major characteristic peaks of zeolite compound coating were detected at 21.3°- (5 3 1), 23.0° - (6 0 0), 25.71°- (6 4 0), 27.7°- (6 4 2), 29.8°- (6 4 4), 32.05°- (8 4 0), 35.3°- (8 8 4), 41.5°- (8 8 0) [72–74]. XRD study confirms the formation of appropriate crystalline Na-based ZSM-5. The average crystalline size was calculated using the Scherrer equation by considering the most dominant peak detected at $2\theta = 23.0^{\circ}$ associated with lattice plane (6 0 0), and it is around 44.85 nm. However, there was not much difference detected with the XRD peaks of zeolite-coated fs laser and ps laser fabricated surfaces.

The morphology of zeolite-coated bare and laser fabricated surfaces is shown in Fig. S7. After the zeolite coating, the fabricated surfaces possess uniform depth. The submicron roughness allows zeolite to attach to the surface efficiently. The wetting behaviours of the zeolite-coated bare and laser fabricated surfaces are evaluated using contact angle measurements. The measured contact angle on the coated bare sample ($5.5^0 \pm 1.25$ ms) exhibits $\sim$ 91% – 95% reduction from that of a bare sample without coating (shown in Fig. 14 (a, b)), which is not a complete wicking surface. However, it demonstrated the ability of the zeolite coating to absorb water molecules, which is consistent with the reported studies of zeolite coating (by *McDonnell et. al.*) on similar metal surfaces such as Al alloy and stainless steel [67]. Interestingly as shown in Fig. 14 (c-f), the zeolite coated laser fabricated surface clearly shows complete wicking of a water droplet and quickly formed a thin film with almost 0^o contact angle and spreading time of 370 ms and 300 ms for fs and ps laser fabricated surfaces respectively with ± 10 ms error bar (spreading

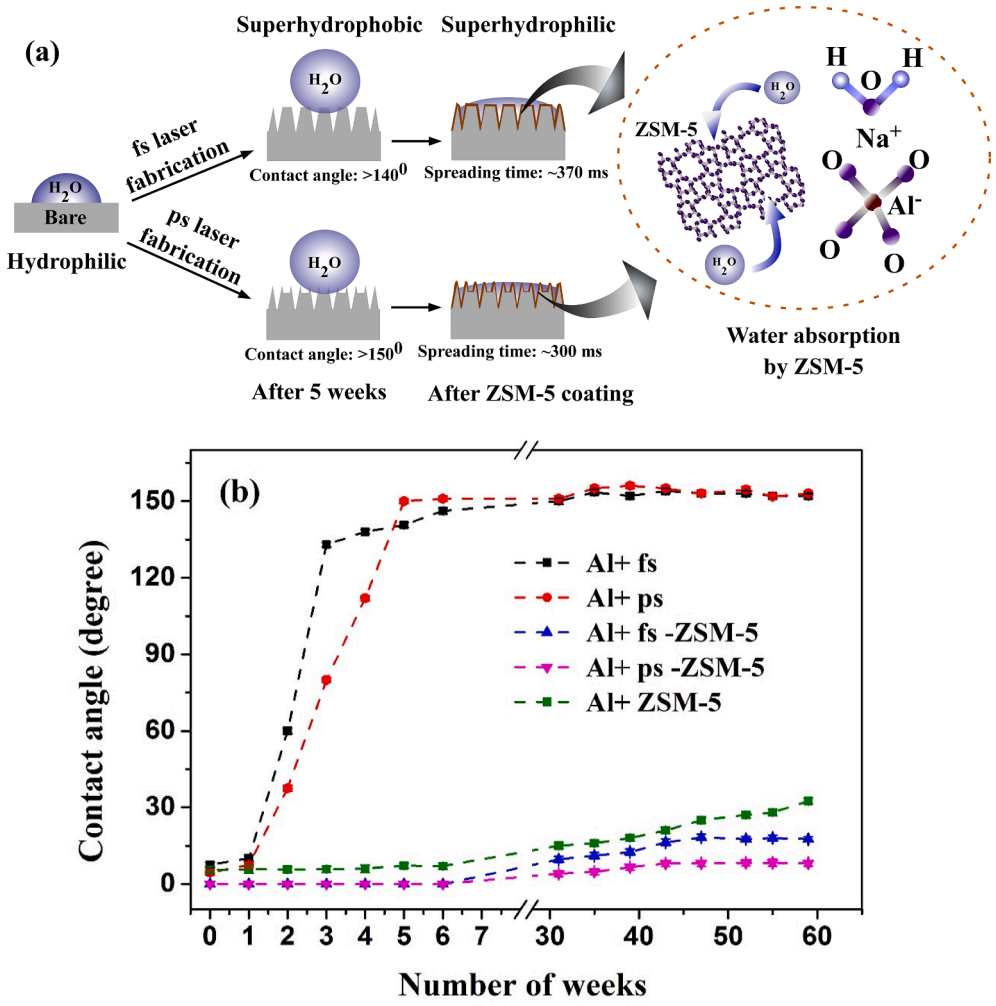

Fig. 15. (a) Schematic illustration shows the wettability transition happened to the bare Al surface after 35 days of laser fabrication and after subsequent zeolite coating (water imbibition mechanism of ZSM-5 also shown). (b) Shows the surface wettability evolution of the studied samples in around 60 weeks of time.

time measured on five different positions on the surface and averaged).

A schematic illustration of water adsorption by the zeolite-coated laser fabricated surface is shown in Fig. 15 (a). Various studies carried out on the water adsorption by Na-based ZSM-5 show that initially, water molecules are adsorbed by the Na^+ cations and Al atoms present in the zeolite framework surface superhydrophilic [68,74–77]. Besides, the laser fabricated micro-capillary channels and their intense wicking action makes the surface super-wicking. Thus, the real wetting property of the laser fabricated superhydrophilic surface is reversed. This wetting transition from non-wetting to wetting is called Cassie to Wenzel state transition [78]. Fig. 15 (b) depicts the long-term superhydrophilic stability of the zeolite-coated samples for more than 14 months. When time progresses, the contact angle of zeolite coated fs laser fabricated surface slowly increasing. However, the ps laser fabricated surface shown excellent long-term wetting stability (contact angle less than 10°). It reveals the importance of zeolite coating on ps laser fabricated surfaces with optimum laser parameters (120 mW laser power, 20 μm step size, and 0.75 mm/s to 1.25 mm/s scanning speed) for long-term stable superhydrophilic behaviour.

4. Conclusion

A comparison of fs laser and ps laser fabricated hierarchical superhydrophilic surface structures on Al was investigated in this work. Combinations of extensive laser parameter variations such as laser power (40 mW, 80 mW, and 120 mW), scanning velocity (0.1 mm/s to 5.0 mm/s), and step sizes (20 μm, 60 μm, 110 μm, and 160 μm) were used to guarantee a wide range of experimental results. The results subdivided into two parts; the first section discussed these laser parameters' effect on resultant surface roughness factors related to micro-nano structures and their role in surface wettability. The second part examined the variation of surface chemistry related to molecular compositions on structured surfaces.

In the first section, SEM analysis was used to investigate the morphology of sample surfaces in detail. It showed high power-structured surfaces with high aspect ratio capillary grooves, nanoparticles, and micro-cracks give rise to highly efficient superhydrophilic surfaces that demonstrated 0° contact angle and fast-spreading of 300 ms. Besides, regular and uniform microcapillary grooves fabricated with the optimum step sizes and laser scanning speeds and ps laser pulses also exhibited superior wetting behaviour than other surfaces.

A comprehensive investigation of surface chemistry was carried out with EDS, XRD, and FTIR analysis in the second part. EDS and XRD analysis investigated the amount of Al_2O_3 formation for various laser parameters. It confirmed that better superhydrophilic surfaces (0° of contact angle with 300 ms of spreading time) were fabricated by higher ps laser power (120 mW) combined with lower step size (20 μm) and optimum scanning speed (0.75 mm/s- 1.25 mm/s).

Nevertheless, the significant FTIR analysis studied the amount of chemisorbed organic, hydroxyl (–OH), and C-C(H) functional group contamination on fabricated surfaces over time. It indicated that the

laser fabricated superwiking capillary grooves with a high aspect ratio transferred into strong air pockets and preventing the surface from wetting in around five weeks. In addition, we coated the Na-based ZSM-5 on fabricated surfaces to maintain the superhydrophilic property for more than 14 months. The findings propose an approach to manufacture long-term stable superhydrophilic metal surfaces for microfluidics devices, water splitting surfaces, and anti-corrosive wetting surfaces.

CRediT authorship contribution statement

Rahul A. Rajan: Conceptualization, Data curation, Investigation, Methodology. **Chi-Vinh Ngo:** Conceptualization, Supervision. **J. Yang:** Supervision. **Yu Liu:** Investigation. **K.S. Rao:** Resources. **Chunlei Guo:** Funding acquisition, Project administration.

Declaration of Competing Interest

The authors declare that they have no known competing financial interests or personal relationships that could have appeared to influence the work reported in this paper.

Acknowledgment

This work was supported by National Natural Science Foundation of China (Grant No. 91750205, 11674178, 11804334), Bill & Melinda Gates Foundation (OPP1157723), Chinese Academy of Sciences President's International Fellowship Initiative (Grant No. 2019PE0010), Strategic Priority Research Program of Chinese Academy of Sciences (XDA22010302), Jilin Provincial Science & Technology Development Project (Grant No. 20180414019GH), K.C.Wong Education Foundation (Grant No. GJTD-2018-08). Rahul A. Rajan gratefully acknowledges his support from UCAS Full-Fellowship for International Students (20190442) and Dr. Saji K. J, Dr. Hamad Sayed for their initial discussions, and Gan Yuan for his help to take XRD data.

Appendix A. Supplementary material

Supplementary data to this article can be found online at https://doi.org/10.1016/j.optlastec.2021.107241.

References

[1] S.C. Singh, M. ElKabbash, Z. Li, X. Li, B. Regmi, M. Madsen, S.A. Jalil, Z. Zhan, J. Zhang, C. Guo, Solar-trackable super-wicking black metal panel for photothermal water sanitation, Nat. Sustain. 3 (2020) 938–946, https://doi.org/10.1038/s41893-020-0566-x.
[2] J. Lu, C.V. Ngo, S.C. Singh, J. Yang, W. Xin, Z. Yu, C. Guo, Bioinspired Hierarchical Surfaces Fabricated by Femtosecond Laser and Hydrothermal Method for Water Harvesting, Langmuir 35 (2019) 3562–3567, https://doi.org/10.1021/acs.langmuir.8b04295.
[3] J. Zhang, C. Zhang, J. Sha, H. Fei, Y. Li, J.M. Tour, Efficient Water-Splitting Electrodes Based on Laser-Induced Graphene, ACS Appl. Mater. Interfaces. 9 (2017) 26840–26847, https://doi.org/10.1021/acsami.7b06727.
[4] G. Chitnis, Z. Ding, C.L. Chang, C.A. Savran, B. Ziaie, Laser-treated hydrophobic paper: An inexpensive microfluidic platform, Lab Chip. 11 (2011) 1161–1165, https://doi.org/10.1039/c0lc00512f.
[5] W. Barthlott, C. Neinhuis, Purity of the sacred lotus, or escape from contamination in biological surfaces, Planta 202 (1997) 1–8, https://doi.org/10.1007/s004250050096.
[6] K. Koch, I.C. Blecher, G. König, S. Kehraus, W. Barthlott, The superhydrophilic and superoleophilic leaf surface of Ruellia devosiana (Acanthaceae): A biological model for spreading of water and oil on surfaces, Funct. Plant Biol. 36 (2009) 339–350, https://doi.org/10.1071/FP08295.
[7] K. Koch, W. Barthlott, Superhydrophobic and superhydrophilic plant surfaces: An inspiration for biomimetic materials, Philos. Trans. R. Soc. A Math. Phys. Eng. Sci. 367 (2009) 1487–1509, https://doi.org/10.1098/rsta.2009.0022.
[8] A.R. Parker, C.R. Lawrence, Water capture by a desert beetle, Nature 414 (2001) 33–34, https://doi.org/10.1038/35102108.
[9] S.F. Toosi, S. Moradi, M. Ebrahimi, S.G. Hatzikiriakos, Microfabrication of polymeric surfaces with extreme wettability using hot embossing, Appl. Surf. Sci. 378 (2016) 426–434, https://doi.org/10.1016/j.apsusc.2016.03.116.
[10] R.V. Lakshmi, B.J. Basu, Fabrication of superhydrophobic sol-gel composite films using hydrophobically modified colloidal zinc hydroxide, J. Colloid Interface Sci. 339 (2009) 454–460, https://doi.org/10.1016/j.jcis.2009.07.064.
[11] J. Cremaldi, B. Bhushan, Fabrication of bioinspired, self-cleaning superliquiphilic/phobic stainless steel using different pathways, J. Colloid Interface Sci. 518 (2018) 284–297, https://doi.org/10.1016/j.jcis.2018.02.034.
[12] S.A. Ahmad Kamal, R. Ritikos, S. Abdul Rahman, Wetting behaviour of carbon nitride nanostructures grown by plasma enhanced chemical vapour deposition technique, Appl. Surf. Sci. 328 (2015) 146–153, https://doi.org/10.1016/j.apsusc.2014.12.001.
[13] Y. Liu, S. Li, Y. Wang, H. Wang, K. Gao, Z. Han, L. Ren, Superhydrophobic and superoleophobic surface by electrodeposition on magnesium alloy substrate: Wettability and corrosion inhibition, J. Colloid Interface Sci. 478 (2016) 164–171, https://doi.org/10.1016/j.jcis.2016.06.006.
[14] S. Zhang, X. Zeng, D.T.A. Matthews, A. Igartua, E. Rodriguez-Vidal, J. Contreras Fortes, V. Saenz de Viteri, F. Pagano, B. Wadman, E.D. Wiklund, E. van der Heide, Selection of micro-fabrication techniques on stainless steel sheet for skin friction, Friction. 4 (2016) 89–104, https://doi.org/10.1007/s40544-016-0115-9.
[15] Z. Yang, Y. Tian, Y. Zhao, C. Yang, Study on the fabrication of super-hydrophobic surface on Inconel Alloy via nanosecond laser ablation, Materials (Basel). 12 (2019) 278, https://doi.org/10.3390/ma12020278.
[16] Y. Song, C. Wang, X. Dong, K. Yin, F. Zhang, Z. Xie, D. Chu, J. Duan, Controllable superhydrophobic aluminum surfaces with tunable adhesion fabricated by femtosecond laser, Opt. Laser Technol. 102 (2018) 25–31, https://doi.org/10.1016/j.optlastec.2017.12.024.
[17] Z. Ma, C. Li, X. Hu, B. Han, Y. Zhang, Q. Chen, Laser Fabrication of Bioinspired Graphene Surfaces With Superwettability, Front Chem. 8 (2020) 1–6, https://doi.org/10.3389/fchem.2020.00525.
[18] A.I. Carim, N.A. Batara, A. Premkumar, H.A. Atwater, N.S. Lewis, Polarization control of morphological pattern orientation during light-mediated synthesis of nanostructured se-Te films, ACS Nano 10 (2016) 102–111, https://doi.org/10.1021/acsnano.5b05119.
[19] D. Zhang, B. Ranjan, T. Tanaka, K. Sugioka, Underwater persistent bubble-assisted femtosecond laser ablation for hierarchical micro/nanostructuring, Int. J. Extrem. Manuf. 2 (2020) 15001, https://doi.org/10.1088/2631-7990/ab729f.
[20] Á. Cubero, E. Martínez, L.A. Angurel, G.F. de la Fuente, R. Navarro, H. Legall, J. Krüger, J. Bonse, Surface superconductivity changes of niobium sheets by femtosecond laser-induced periodic nanostructures, Nanomaterials. 10 (2020) 1–16, https://doi.org/10.3390/nano10122525.
[21] E. Stratakis, J. Bonse, J. Heitz, J. Siegel, G.D. Tsibidis, E. Skoulas, A. Papadopoulos, A. Mimidis, A.C. Joel, P. Comanns, J. Krüger, C. Florian, Y. Fuentes-Edfuf, J. Solis, W. Baumgartner, Laser engineering of biomimetic surfaces, Mater. Sci. Eng. R Reports. 141 (2020), 100562, https://doi.org/10.1016/j.ijleo.2020.165726.
[22] R. Stoian, J.P. Colombier, Advances in ultrafast laser structuring of materials at the nanoscale, Nanophotonics. 9 (2020) 4665–4688, https://doi.org/10.1515/nanoph-2020-0310.
[23] D. Zhang, L.C. Wu, M. Ueki, Y. Ito, K. Sugioka, Femtosecond laser shockwave peening ablation in liquids for hierarchical micro/nanostructuring of brittle silicon and its biological application, Int. J. Extrem. Manuf. 2 (2020) 045001, https://doi.org/10.1088/2631-7990/abb5f3.
[24] J.J.J. Nivas, E. Allahyari, A. Vecchione, Q. Hao, S. Amoruso, X. Wang, Laser ablation and structuring of CdZnTe with femtosecond laser pulses, J. Mater. Sci. Technol. 48 (2020) 180–185, https://doi.org/10.1016/j.jmst.2020.01.059.
[25] A.M. Kietzig, S.G. Hatzikiriakos, P. Englezos, Patterned superhydrophobic metallic surfaces, Langmuir 25 (2009) 4821–4827, https://doi.org/10.1021/la8037582.
[26] C. Florian, S.V. Kirner, J. Krüger, J. Bonse, Surface functionalization by laser-induced periodic surface structures, J. Laser Appl. 32 (2020), 022063, https://doi.org/10.2351/7.0000103.
[27] Y.H. Liu, Y.K. Tseng, C.W. Cheng, Direct fabrication of rotational femtosecond laser-induced periodic surface structure on a tilted stainless steel surface, Opt. Laser Technol. 134 (2021), 106648, https://doi.org/10.1016/j.optlastec.2020.106648.
[28] Y.C. Guan, F.F. Luo, G.C. Lim, M.H. Hong, H.Y. Zheng, B. Qi, Fabrication of metallic surfaces with long-term superhydrophilic property using one-stop laser method, Mater. Des. 78 (2015) 19–24, https://doi.org/10.1016/j.matdes.2015.04.021.
[29] E. Kostal, S. Stroj, S. Kasemann, V. Matylitsky, M. Domke, Fabrication of Biomimetic Fog-Collecting Superhydrophilic-Superhydrophobic Surface Micropatterns Using Femtosecond Lasers, Langmuir 34 (2018) 2933–2941, https://doi.org/10.1021/acs.langmuir.7b03699.
[30] A.Y. Vorobyev, C. Guo, Direct femtosecond laser surface nano/microstructuring and its applications, Laser Photonics Rev. 7 (2013) 385–407, https://doi.org/10.1002/lpor.201200017.
[31] K. Ding, M. Li, C. Wang, N. Lin, H. Wang, Z. Luo, J. Duan, Sequential Evolution of Colored Copper Surface Irradiated by Defocused Femtosecond Laser, Adv. Eng. Mater. 22 (2020) 1–9, https://doi.org/10.1002/adem.201901310.
[32] K. Ding, C. Wang, Y. Zheng, Z. Xie, Z. Luo, S. Man, B. Wu, J. Duan, One-step fabrication of multifunctional fusiform hierarchical micro/nanostructures on copper by femtosecond laser, Surf. Coatings Technol. 367 (2019) 244–251, https://doi.org/10.1016/j.surfcoat.2019.04.005.
[33] E. Forrest, R. Schulze, C. Liu, D. Dombrowski, Influence of surface contamination on the wettability of heat transfer surfaces, Int. J. Heat Mass Transf. 91 (2015) 311–317, https://doi.org/10.1016/j.ijheatmasstransfer.2015.07.112.
[34] B. Zheng, G. Jiang, W. Wang, X. Mei, Fabrication of superhydrophilic or superhydrophobic self-cleaning metal surfaces using picosecond laser pulses and

chemical fluorination, Radiat. Eff. Defects Solids. 171 (2016) 461–473, https://doi.org/10.1080/10420150.2016.1211658.
[35] Z. Yang, X. Liu, Y. Tian, Insights into the wettability transition of nanosecond laser ablated surface under ambient air exposure, J. Colloid Interface Sci. 533 (2019) 268–277, https://doi.org/10.1016/j.jcis.2018.08.082.
[36] J. Long, M. Zhong, P. Fan, D. Gong, H. Zhang, Wettability conversion of ultrafast laser structured copper surface, J. Laser Appl. 27 (2015) S29107, https://doi.org/10.2351/1.4906477.
[37] S.A. Khan, V. Ialyshev, V.V. Kim, M. Iqbal, H. Al Harmi, G.S. Boltaev, R.A. Ganeev, A.S. Alnaser, Expedited Transition in the Wettability Response of Metal Meshes Structured by Femtosecond Laser Pulses for Oil-Water Separation, Front. Chem. 8 (2020) 1–11, https://doi.org/10.3389/fchem.2020.00768.
[38] A.O. Ijaola, E.A. Bamidele, C.J. Akisin, I.T. Bello, A.T. Oyatobo, A. Abdulkareem, P. K. Farayibi, E. Asmatulu, Wettability Transition for Laser Textured Surfaces: A Comprehensive Review, Surf. Interfaces 21 (2020), 100802, https://doi.org/10.1016/j.surfin.2020.100802.
[39] F. Xie, J. Yang, C.V. Ngo, The effect of femtosecond laser fluence and pitches between V-shaped microgrooves on the dynamics of capillary flow, Results Phys. 19 (2020), 103606, https://doi.org/10.1016/j.rinp.2020.103606.
[40] A.Y. Vorobyev, C. Guo, Metal pumps liquid uphill, Appl. Phys. Lett. 94 (2009) 2007–2010, https://doi.org/10.1063/1.3117237.
[41] A.Y. Vorobyev, C. Guo, Laser Makes Silicon Superwicking, Opt. Photonics News. 21 (2010) 38, https://doi.org/10.1364/opn.21.12.000038.
[42] A.Y. Vorobyev, C. Guo, Water sprints uphill on glass, J. Appl. Phys. 108 (2010) 123512, https://doi.org/10.1063/1.3511431.
[43] A. Gabler, C.I. Müller, T. Rauscher, T. Gimpel, R. Hahn, M. Köhring, B. Kieback, L. Röntzsch, W. Schade, Ultrashort-pulse laser structured titanium surfaces with sputter-coated platinum catalyst as hydrogen evolution electrodes for alkaline water electrolysis, Int. J. Hydrogen Energy. 43 (2018) 7216–7226, https://doi.org/10.1016/j.ijhydene.2018.02.130.
[44] X. Cheng, Z. Wang, Y. Yan, Corrosion-resistant zeolite coatings by in situ crystallization, Electrochem. Solid-State Lett. 4 (2001) 23–26, https://doi.org/10.1149/1.1359396.
[45] P. Chakraborty Banerjee, R.P. Woo, S.M. Grayson, A. Majumder, R.K. Singh Raman, Influence of zeolite coating on the corrosion resistance of AZ91D magnesium alloy, Materials (Basel) 7 (2014) 6092–6104, https://doi.org/10.3390/ma7086092.
[46] R.N. Wenzel, Resistance of solid surfaces to wetting by water, Ind. Eng. Chem. 28 (1936) 988–994, https://doi.org/10.1021/ie50320a024.
[47] B.N. Chichkov, C. Momma, S. Nolte, F. von Alvensleben, A. Tünnermann, Femtosecond, picosecond and nanosecond laser ablation of solids, Appl. Phys. A Mater. Sci. Process. 63 (1996) 109–115, https://doi.org/10.1007/s003390050359.
[48] T.L.P.S.I. Anisimov, B.L. Kapeliovich, Electron emission from metal surfaces exposed to ultrashort laser pulses, J. Exp. Theor. Phys. 39 (1974) 776–781, https://doi.org/10.1051/rphysap:01977001205078900.
[49] K.H. Leitz, B. Redlingshöer, Y. Reg, A. Otto, M. Schmidt, Metal ablation with short and ultrashort laser pulses, Phys. Procedia. 12 (2011) 230–238, https://doi.org/10.1016/j.phpro.2011.03.128.
[50] C. Zhang, L. Cheng, B. Tan, Z. Chen, W. Zhang, Z. Liu, J. Peng, Directional liquid spreading on laser textured aluminum surface, Microsyst. Technol. 26 (2020) 2767–2776, https://doi.org/10.1007/s00542-020-04914-6.
[51] N.N. Nedialkov, P.A. Atanasov, S. Amoruso, R. Bruzzese, X. Wang, Laser ablation of metals by femtosecond pulses: Theoretical and experimental study, Appl. Surf. Sci. 253 (2007) 7761–7766, https://doi.org/10.1016/j.apsusc.2007.02.083.
[52] S.M. Eaton, H. Zhang, P.R. Herman, F. Yoshino, L. Shah, J. Bovatsek, A.Y. Arai, Heat accumulation effects in femtosecond laser-written waveguides with variable repetition rate, Opt. Express. 13 (2005) 4708, https://doi.org/10.1364/opex.13.004708.
[53] M.E.A. Ben Amara, S. Ben Nasrallah, Capillary rise in a non-uniform tube, J. Porous Media. 14 (2011) 411–422, https://doi.org/10.1615/JPorMedia.v14.i5.40.
[54] P. Li, J. Xie, Z. Deng, Characterization of irregularly micro-structured surfaces related to their wetting properties, Appl. Surf. Sci. 335 (2015) 29–38, https://doi.org/10.1016/j.apsusc.2015.01.220.
[55] Y. Tsori, Discontinuous liquid rise in capillaries with varying cross-sections, Langmuir 22 (2006) 8860–8863, https://doi.org/10.1021/la061605x.
[56] H. Zhu, H. Zhang, X. Ni, Z. Shen, J. Lu, Fabrication of superhydrophilic surface on metallic nickel by sub-nanosecond laser-induced ablation, AIP Adv. 9 (2019), https://doi.org/10.1063/1.5111069.
[57] J.E. Castle, The composition of metal surfaces after atmospheric exposure: An historical perspective, J. Adhes. 84 (2008) 368–388, https://doi.org/10.1080/00218460802004477.
[58] C.V. Ngo, D.M. Chun, Control of laser-ablated aluminum surface wettability to superhydrophobic or superhydrophilic through simple heat treatment or water boiling post-processing, Appl. Surf. Sci. 435 (2018) 974–982, https://doi.org/10.1016/j.apsusc.2017.11.185.
[59] M.J. Kong, S.S. Lee, J. Lyubovitsky, S.F. Bent, Infrared spectroscopy of methyl groups on silicon, Chem. Phys. Lett. 263 (1996) 1–7, https://doi.org/10.1016/S0009-2614(96)01186-4.
[60] R.G. Snyder, H.L. Strauss, C.A. Elliger, C-H stretching modes and the structure of n-alkyl chains. 1. Long, disordered chains, J. Phys. Chem. 86 (1982) 5145–5150, https://doi.org/10.1021/j100223a018.
[61] J. Zhang, H. Tsuji, I. Noda, Y. Ozaki, Weak intermolecular interactions during the melt crystallization of poly(L-lactide) investigated by two-dimensional infrared correlation spectroscopy, J. Phys. Chem. B. 108 (2004) 11514–11520, https://doi.org/10.1021/jp048308q.
[62] M. Namvari, H. Namazi, Sweet graphene I: Toward hydrophilic graphene nanosheets via click grafting alkyne-saccharides onto azide-functionalized graphene oxide, Carbohydr. Res. 396 (2014) 1–8, https://doi.org/10.1016/j.carres.2014.06.012.
[63] L.M. Sanz-Moral, M. Rueda, A. Nieto, Z. Novak, Ž. Knez, Á. Martín, Gradual hydrophobic surface functionalization of dry silica aerogels by reaction with silane precursors dissolved in supercritical carbon dioxide, J. Supercrit. Fluids. 84 (2013) 74–79, https://doi.org/10.1016/j.supflu.2013.09.010.
[64] Q. Zhang, D. Xu, T.F. Hung, K. Zhang, Facile synthesis, growth mechanism and reversible superhydrophobic and superhydrophilic properties of non-flaking CuO nanowires grown from porous copper substrates, Nanotechnology. 065602 (2013), https://doi.org/10.1088/0957-4484/24/6/065602.
[65] Y. Zhu, J.C. Zhang, J. Zhai, L. Jiang, Preparation of superhydrophilic α-Fe2O3 nanofibers with tunable magnetic properties, Thin Solid Films 510 (2006) 271–274, https://doi.org/10.1016/j.tsf.2005.09.004.
[66] T. Nakatani, K. Okamoto, I. Omura, S. Yamashita, Imparting superhydrophilicity to diamond-like carbon by plasma surface treatment technique, New Diam. Front. Carbon Technol. 17 (2007) 289–300.
[67] A.M.P. McDonnell, D. Beving, A. Wang, W. Chen, Y. Yan, Hydrophilic and antimicrobial zeolite coatings for gravity-independent water separation, Adv. Funct. Mater. 15 (2005) 336–340, https://doi.org/10.1002/adfm.200400183.
[68] A. Jentys, G. Warecka, M. Derewinski, J.A. Lercher, Adsorption of water on ZSM5 zeolites, J. Phys. Chem. 93 (1989) 4837–4843, https://doi.org/10.1021/j100349a032.
[69] G. Giannetto, L. García, J. Papa, F. Yánez, M.R. Goldwasser, C. Linares, D. Moronta, B. Mendez, C. Urbina De Navarro, R. Monque, Synthesis and characterization of [Cr, AI]-ZSM-5 zeolites, Zeolites 19 (1997) 169–174, https://doi.org/10.1016/S0144-2449(97)00064-X.
[70] D. Scarano, A. Zecchina, S. Bordiga, F. Geobaldo, G. Spoto, E. Anic, C. Ricerche, S. Pietro, Fourier-transform Infrared and Raman Spectra of Pure and Al-, B-, Ti- and Fe-substituted Silicalites : Stretching-mode Region, J. Chem. Soc. Faraday Trans. 89 (1993) 4123–4130.
[71] Y.K. Rohayati, R. Krisnandi, Sihombing, Synthesis of ZSM-5 zeolite using Bayat natural zeolite as silica and alumina source, AIP Conf. Proc. 2017 (1862) 1–5, https://doi.org/10.1063/1.4991198.
[72] F. Zamani, M. Rezapour, S. Kianpour, Immobilization of L-Lysine on zeolite 4A as an organic-inorganic composite basic catalyst for synthesis of α, β-unsaturated carbonyl compounds under mild conditions, Bull. Korean Chem. Soc. 34 (2013) 2367–2374, https://doi.org/10.5012/bkcs.2013.34.8.2367.
[73] R.S. Khairnar, M.D. Wakde, M.P. Mahabole, R. Krishna, E. Titus, Development of Ethanol Sensor using Sodium A Nano Zeolite, Int. J. Eng. Innov. Technol. 3 (2014) 306–310.
[74] X.D. Guo, S.P. Huang, J.W. Teng, Z.K. Xie, Study on the adsorption of water on NanZSM-5 type zeolite: Molecular simulation, Acta Phys. - Chim. Sin. 22 (2006) 270–274, https://doi.org/10.1016/S1872-1508(06)60001-6.
[75] L. Ohlin, V. Berezovsky, S. Öberg, A. Farzaneh, A. Holmgren, M. Grahn, Effect of Water on the Adsorption of Methane and Carbon Dioxide in Zeolite Na-ZSM-5 Studied Using in Situ ATR-FTIR Spectroscopy, J. Phys. Chem. C. 120 (2016) 29144–29152, https://doi.org/10.1021/acs.jpcc.6b09224.
[76] T. Ohgushi, S. Kataoka, Kinds of cations in NaZSM-5 zeolite, J. Colloid Interface Sci. 148 (1992) 148–154, https://doi.org/10.1016/0021-9797(92)90122-3.
[77] B. Hunger, M. Heuchel, S. Matysik, K. Beck, W.D. Einicke, Adsorption of water on ZSM-5 zeolites, Thermochim. Acta. 269–270 (1995) 599–611, https://doi.org/10.1016/0040-6031(95)02541-3.
[78] X. Feng, L. Jiang, Design and creation of superwetting/antiwetting surfaces, Adv. Mater. 18 (2006) 3063–3078, https://doi.org/10.1002/adma.200501961.